

**Monte Carlo simulations of hole dynamics in SiGe/Si terahertz quantum-cascade structures**

Z. Ikončić,\* R. W. Kelsall, and P. Harrison

*Institute of Microwaves and Photonics, School of Electronic and Electrical Engineering, University of Leeds, Leeds LS2 9JT, United Kingdom*

(Received 5 December 2003; revised manuscript received 22 March 2004; published 10 June 2004)

A detailed analysis of hole transport in cascaded  $p$ -Si/SiGe quantum well structures is performed using ensemble Monte Carlo simulations. The hole subband structure is calculated using the  $6 \times 6 \mathbf{k} \cdot \mathbf{p}$  model, and then used to find carrier relaxation rates due to the alloy disorder, acoustic and optical phonon scattering. The simulation accounts for the in-plane  $\mathbf{k}$ -space anisotropy of both the hole subband structure and the scattering rates. Results are presented for prototype terahertz Si/SiGe quantum cascade structures.

DOI: 10.1103/PhysRevB.69.235308

PACS number(s): 73.63.Hs, 85.35.Be

**I. INTRODUCTION**

There has recently been an increased interest in intersubband transitions in  $p$ -type strained-layer SiGe based quantum wells, due to their possible use in intersubband quantum cascade lasers operating from near- to far-infrared wavelength ranges. This is largely related to the fact that hole intersubband transitions are optically active for both the perpendicular and the in-plane polarization of light, hence enabling the realization of surface emitting intersubband lasers. These points, together with the possibility of monolithic integration of silicon-based electronic and optoelectronic components, are strong incentives for the development of a SiGe quantum cascade laser. Following the earlier proposals of suitable structures,<sup>1,2</sup> considerable research effort has been devoted to this problem. Currently there are reports on successful growth of long Si/SiGe cascades, and electroluminescence has been observed in both the midinfrared<sup>3,4</sup> and far-infrared<sup>5,6</sup> wavelength ranges, although full laser operation has yet to be achieved. Bias-tunable emission wavelength has also been demonstrated<sup>7</sup> (as well as tunable absorption wavelength in detectors<sup>8</sup>).

Understanding the carrier dynamics is an important issue for the design of quantum cascade lasers (QCL's), the gain depending on the scattering between different subbands and also between different in-plane momentum states within a subband. This has been extensively studied in QCL's based on conduction-band intersubband transitions. One approach relies on self-consistent solution of rate equations of different levels of sophistication.<sup>9-13</sup> Another uses microscopic, and computationally more demanding, methods based on the Boltzmann equation,<sup>14</sup> which employ the Monte Carlo (MC) technique<sup>15-19</sup> (similar MC simulations have also been performed for optically pumped intersubband lasers<sup>20</sup>). While the rate equation methods give reasonably good estimates of device characteristics, they rely on the assumption of equilibriumlike carrier distributions over states within any single subband. In contrast, the MC method does not involve any such assumption, and gives a deeper insight into the carrier dynamics.

While there have been detailed theoretical studies of hole transport in quantum confined Si/SiGe systems,<sup>21,22</sup> based on fully anisotropic  $6 \times 6 \mathbf{k} \cdot \mathbf{p}$  description of the subband structure, these have focused on in-plane transport, and there

has been no work on vertical transport in  $p$ -type quantum-cascade structures in any material system. The problem is generally similar to the case of  $n$ -type cascades, but is more complex because the subband structure and scattering rates are anisotropic and strongly dependent on the in-plane momentum of the hole states. Here we describe an implementation of the MC method for calculating hole dynamics in  $p$ -SiGe quantum-cascade structures.

**II. CALCULATION DETAILS**

The cascade is a stack of a number (typically around 100) of unit cells, or periods, each of which may be structurally simple, comprising a single quantum well and barrier, or quite complex. To perform simulations of hole dynamics, the valence subbands of a biased cascade have first to be calculated. Their wave functions are usually localized in a single period of the cascade. In a long cascade the states show quasiperiodicity; i.e., by translating the wave function of a state by one period, and shifting its energy by the potential drop across one period, another actual state of the system (the one mostly localized in the next period) is obtained. Having a set of states assigned to a particular (hereafter called the central, or book-keeping) period, the corresponding sets assigned to other periods may be constructed simply by using quasiperiodicity.

For hole transport calculation the scattering rates between all combinations of states in the cascade are needed: i.e., either between states within a period or between those which belong to different periods (hence state energies and wave functions for all of them are required). In the latter case, only scattering processes between adjacent periods are considered ("nearest-neighbor approximation"<sup>16</sup>), because there is normally a very small overlap of wave functions belonging to more distant periods. To make the problem tractable, the number of states assigned to a single period must be limited, based on the expectation that high-energy states will be virtually unpopulated, because most of the carriers will scatter into lower-energy states of subsequent periods rather than remaining in ever higher states as they move along the cascade. "Periodic boundary conditions" are also used: the particle distribution over states assigned to a period is assumed identical for all periods of the cascade. It is then sufficient to

account explicitly only for particles in a single period, rather than in the whole cascade, and “fold back” the carriers which have scattered out of the book-keeping period. For example, the carriers which have scattered out to the right are replaced with those which have scattered in from the left.

### A. Hole subband structure

The hole band structure is calculated using the  $6 \times 6 \mathbf{k} \cdot \mathbf{p}$  scheme in the plane wave implementation, as described previously,<sup>23</sup> using Foreman’s boundary conditions.<sup>24</sup> The accuracy of the method is good for the class of structures of interest in this work,<sup>25</sup> although for midinfrared cascades, which involve higher transition energies and therefore larger in-plane wave vectors ( $\mathbf{k}_{\parallel}$ ) involved in scattering, it may be necessary to include more bands and use, e.g., the recently developed  $14 \times 14 \mathbf{k} \cdot \mathbf{p}$  model.<sup>26</sup> For the scattering rates calculation one would then also need the hole-phonon coupling Hamiltonian and its parameters, beyond those established for the  $6 \times 6 \mathbf{k} \cdot \mathbf{p}$  model, so the latter seems a reasonable choice at present. The energies and wave functions of the subbands of interest are tabulated at a number of  $\mathbf{k}_{\parallel}$  values in the irreducible wedge of the two-dimensional (2D) Brillouin zone (for the usual, [001] grown structures this is 1/8 of the full 2D Brillouin zone), and the symmetry properties are used to reconstruct states outside this wedge by rotation. For *electrons* one would just find the set of states at  $\mathbf{k}_{\parallel}=0$ , and use these wave functions for any value of  $\mathbf{k}_{\parallel}$ , while the energy then acquires the in-plane kinetic contribution of  $\hbar^2 k_{\parallel}^2 / 2m^*$ , where the electron effective mass  $m^*$  is assumed to be constant. This approximation cannot be used for *holes*: mixing of heavy-hole (hh), light-hole (lh), and spin-orbit split-off (so) valence band states results in both a prominent in-plane nonparabolicity and anisotropy of hole subbands. A note should be added concerning the (non) degeneracy of the two hole “spin” states. The  $6 \times 6$  Hamiltonian is block diagonalized into two  $3 \times 3$  blocks, and the eigenstates are found for each block, one at a time, because it reduces the computation time by a factor of 4, as compared to solving the full  $6 \times 6$  Hamiltonian. The procedure is exact in bulk materials, but in heterostructures it relies on the position independence of the ratio of Luttinger parameters  $\gamma_3/\gamma_2$ , and to perform it we use the averaged value of  $\gamma_3/\gamma_2$  in the structure. For the case of a symmetric potential the two blocks deliver identical sets of states. However, in a biased cascade the degeneracy is lifted for  $\mathbf{k}_{\parallel} \neq 0$ . The splitting is not very large, typically up to a few meV in the range of  $\mathbf{k}_{\parallel}$  where most of holes reside. This behavior is similar to that of electrons, where the degeneracy of the two spin states is also lifted by the asymmetric potential. The similarity between the electronic and hole “spin” states ends there, however, because electron spin is conserved in all important scattering processes, while hole “spin” (i.e., block) is not: scattering, as well as optical transitions, occurs both within a block or between different blocks.

Tracking particle dynamics in a cascade requires all the states to be assigned to individual periods, generally based on the wave function localization. States in a long cascade are usually found by solving the Schrödinger equation for a

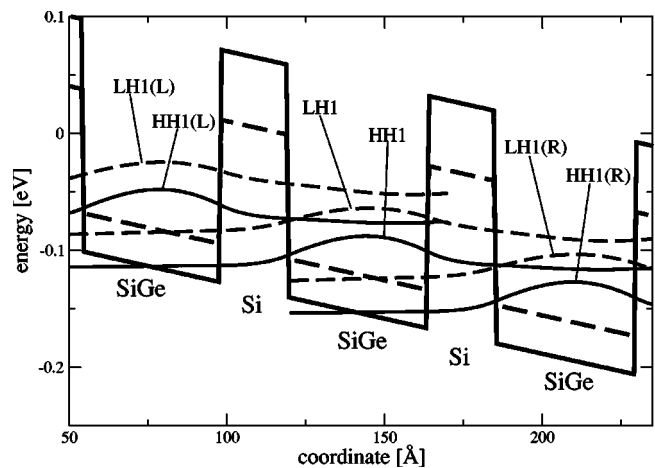


FIG. 1. Relevant hole states in the central and the two adjacent periods of a  $p$ -Si/SiGe cascade comprising 16 monolayer (4.41 nm)  $\text{Ge}_{0.3}\text{Si}_{0.7}$  wells and 8 monolayer (2.15 nm) Si barriers, grown on  $\text{Ge}_{0.2}\text{Si}_{0.8}$  virtual substrate. The wave functions of HH and LH states, as well as the valence band edges for heavy and light holes (different in this strained system), are denoted by solid and dashed lines, respectively. The labels (L) and (R) denote states localized in wells lying to the left and right, respectively, of the “central” well.

three-period-long structure subject to either box or periodic boundary conditions, and appropriately selecting the states from the “middle” of the structure for further work. However, hybridization (anticrossing) of states may occasionally appear, when they are close in energy. If this is of a “cross-period” type, involving two states otherwise localized in two adjacent periods, the two states are about evenly distributed between the two periods. When performing the state assignment, one has to take care of the fact that the hole states which are well separated in energy at  $\mathbf{k}_{\parallel}=0$  may come closer and anticross at some other value of  $\mathbf{k}_{\parallel}$ . If the two states originate from different periods, their anticrossing along some  $\mathbf{k}_{\parallel}$  direction swaps their localization properties. The assignment of states to a period has thus to be done independently for each value of  $\mathbf{k}_{\parallel}$ . Practically, we find the overlaps of states of a triple-period cascade with those of a single period of a cascade (where no cross-period hybridization exists). The states of the former, which show the largest overlaps with states of the latter, are selected and assigned to the central period, so that the “cross-period” hybridization does not lead to double counting of states. The states of adjacent periods are then constructed by applying quasiperiodicity (Fig. 1). This complication is absent in parabolic-dispersion  $n$ -type cascades, where the assignment can be performed simply by visual inspection of the wave functions.

### B. Scattering rate calculation

The absence of polar optical phonon scattering leaves the deformation potential scattering (via acoustic and nonpolar optical modes) as the main inelastic scattering mechanism in SiGe. Optical phonon scattering in the alloy layers is described by assuming three distinct modes, corresponding to

Ge-Ge, Ge-Si, and Si-Si interatomic vibrations, each with its own frequency and deformation potential (the values for Ge-Si mode are assumed to be the average of those for the Ge-Ge and Si-Si), as well as appropriate weight, according to the number of interatomic bonds present in the alloy.<sup>27</sup> For acoustic phonons, on the other hand, the weighted averages of the sound velocities and deformation potentials of Si and Ge are taken. The phonons are considered to be bulklike, and the tensorial, rather than scalar, form of the hole-phonon interaction Hamiltonian is used.<sup>28–31</sup> In quantum well structures this is important for optical,<sup>31</sup> though not so much for acoustic phonon scattering.<sup>32</sup> Optical phonons are assumed to be nondispersive, while acoustic phonons are taken to have linear dispersion; i.e., the quasielastic approximation is not used. Another important scattering mechanism in SiGe is the alloy disorder scattering, which is purely elastic, but, nevertheless, can induce hole transitions between different subbands.<sup>23,33–35</sup>

Due to hole subband's nonparabolicity and anisotropy, the scattering rates are evaluated numerically, using the linear tetrahedron method<sup>21,36–39</sup> of appropriate dimensionality. For alloy scattering the 2D tetrahedron method is required, for acoustic phonon scattering the 3D method is necessary, while for optical phonons the dispersionless approximation results in a degenerate case of 3D tetrahedron integration, so that the 2D method is sufficient.

In this work we do not account for the hole-hole scattering. This would be quite involved at the same level of detail as is used for single-carrier scattering processes (i.e., with nonparabolicity and anisotropy). Since carrier-carrier scattering increases with increasing carrier density, the results obtained here should be valid in the low-density limit.

### C. Monte Carlo simulation

The Monte Carlo simulation uses a cellular scheme, in which the 2D Brillouin zone is subdivided into a grid of phase space cells and, using the band-structure data tabulated on a mesh in the  $\mathbf{k}_{\parallel}$  plane, the microscopic (differential) scattering rates from each cell into any other cell are calculated. The results are stored in a look-up table (each type of scattering process being a separate entry in this table), to be used for the hole trajectory simulations. This approach is known as “cellular automata” or “transition matrix” method,<sup>40–42</sup> and has much larger memory requirements than the conventional MC implementations, but is faster in the limit of a large number of particles and/or long simulation times. This is because, at the time of simulating the individual hole trajectories, the precalculated differential scattering data are used in a manner which does not require much additional calculation, so this costly phase need not be repeated for each hole as the need arises. The computer memory requirements are reduced considerably by using symmetry: for [001] grown structures the scattering rates are calculated only for initial  $\mathbf{k}_{\parallel i}$  states in 1/8 of the 2D Brillouin zone (with the final  $\mathbf{k}_{\parallel f}$  states lying anywhere in the zone). If a hole lies outside the 1/8 segment, its wave vector is folded to fall within it, and the outcome is unfolded to obtain the true wave vector of the final state. Further memory reduction

was obtained by using quasiperiodicity, which relates upstream and downstream scattering rates as  $w(i \rightarrow j(L)) = w(i(R) \rightarrow j)$  (see Fig. 1), so that there is no need to store the  $w(i \rightarrow j(L))$  rates.

The MC code uses a constant time step,<sup>43,44</sup> which is determined initially by inspection of the look-up table. When tracking the hole dynamics, fast linear tetrahedron interpolation<sup>45</sup> in 2D  $\mathbf{k}_{\parallel}$  space is used to construct a subtable of scattering rates from the particular hole state (with the actual value of  $\mathbf{k}_{\parallel i}$ ) into other states (cells). After assembling its entries, multiplied by the time step, into a table of accumulated scattering probabilities, a random number is generated and ranked in this table, wherefrom it is decided whether the particular event is a real scattering or a self-scattering. If it is a real scattering, the ranking simultaneously decides not only the cell that the final state belongs to, but also the type of scattering that occurred. At that stage the Pauli-exclusion-based acceptance or rejection of this event is applied<sup>46</sup> and, if the event is accepted, the precise  $\mathbf{k}_{\parallel f}$  of the final state is then determined.

When simulating hole dynamics in a quantum cascade structure, an arbitrary (e.g., equilibriumlike) initial distribution of holes over the available states in the central period is generated, and implicitly replicated over all periods. To recognize the approach to the steady state, as the system evolves in time, we calculate the overlap of square roots of the distributions (cell populations), normalized to unity, found at two distinct time intervals, and watch for the convergence of this quantity to unity. Due to the inevitable stochastic fluctuations the test must not be performed with two instantaneous distributions, but rather with those averaged over a number ( $\sim 50$ – $100$ ) of time steps. An alternative way of recognizing the steady state might rely on tracking the total entropy of the system.<sup>47</sup>

It is also worth mentioning the problem of parasitic current spikes, discussed for the case of simulations of  $n$ -type QCL's,<sup>19</sup> which appear in narrow bias ranges when hybridization of remote states occurs, opening a new current path. Such events are considered to be unrealistic because remote states' coupling should be destroyed by dephasing. In  $p$ -type cascades the problem appears in a diffuse form, with coupling of states depending on both the bias and the  $\mathbf{k}_{\parallel}$  vector: well-coupled states may appear at appropriate  $\mathbf{k}_{\parallel}$ 's for almost any bias, inducing some excess current rather than a current spike, but it is difficult to eliminate the phenomenon in any rigorous manner.

## III. NUMERICAL RESULTS AND DISCUSSION

MC simulations have been performed for several  $p$ -Si/SiGe quantum cascade structures. In the band-structure calculation the material parameters for Si and Ge were taken from Refs. 48 and 49, and the phonon deformation potentials from Ref. 30 (set C). There is a considerable spread of the reported values of the alloy scattering potential.<sup>35</sup> We have used the value 0.3 eV (normalized to the volume of the primitive cell), because it gave good agreement with measured intersubband relaxation times.<sup>50</sup>

We consider cascades with the simplest possible structure; i.e., stacks of alternating wells and barriers. One such ex-

ample is a structure comprising 16 monolayer (4.41 nm)  $\text{Ge}_{0.3}\text{Si}_{0.7}$  wells and 8 monolayer (2.15 nm wide) Si barriers, grown on a  $\text{Ge}_{0.2}\text{Si}_{0.8}$  virtual substrate. This is a strain-balanced structure, and therefore can be grown with an arbitrarily large number of periods. It has just two low-lying subbands per period, the ground HH1 and the first excited LH1 subband; the next, HH2 subband is sufficiently higher in energy to remain almost inaccessible to holes throughout the range of biases used in the calculation. The LH1-HH1 energy spacing is 27.5 meV, mostly determined by the strain in the quantum well layers. In a biased cascade the alignment of the HH1 state from the “preceding” (higher) well and the LH1 state of the next (lower) well at  $\mathbf{k}_{\parallel}=0$  occurs at a field of 42 kV/cm. However, for finite  $\mathbf{k}_{\parallel}$  the alignment appears at different fields, because of the different dispersions of the HH and LH subbands, so the phenomenon of “resonance” is more diffuse than in  $n$ -type cascades. As the bias varies, the intrawell HH1-LH1 spacing changes only slightly, and most of the potential drop per period manifests in the displacement of the sets of subbands belonging to adjacent periods. The position of subbands at 60 kV/cm bias is shown in Fig. 1.

Such a structure offers potential as an intersubband terahertz laser, where the lasing transition would be the interwell (diagonal)  $\text{HH1} \rightarrow \text{LH1(R)}$  transition, while the intrawell (vertical)  $\text{LH1} \rightarrow \text{HH1}$  is the relaxation transition, emptying the lower laser subband (see Fig. 1 for notation). This is because: (i) the optical matrix element near the zone center, for both in-plane and normally polarized light, is larger for the interwell than for the intrawell transition, and (ii) it is plausible to expect that the upper state will be less populated than the lower state in the same well, which would imply that a population inversion would automatically exist for the interwell transition. The  $\text{HH1} \rightarrow \text{LH1(R)}$  interwell transition energy can be tuned by the bias field: at  $\mathbf{k}_{\parallel}=0$  it is zero at 42 kV/cm, and increases by 6.6 meV for each 10 kV/cm of excess bias.

The results of MC simulations of such a quantum cascade structure are shown in Fig. 2. The population of the LH1 subband has a peak approximately at the HH1-LH1(R) alignment bias (hence the population inversion is worst there, but this is not the working bias for lasing anyway, as explained above). The current generally increases with bias, although there is a broad region of negative differential resistance (NDR). The peak/valley current ratio is very small, which is favorable in respect of avoiding domain formation. Figure 2 also shows the effective temperatures of the holes in the two subbands. The hole distributions obtained from the MC simulation do not correspond to Fermi-Dirac (FD) distributions for any values of hole temperatures, Figs. 3(a) and 3(b). Therefore, the effective temperature of a subband is defined as the temperature which, when used in the FD distribution, gives the same value of total kinetic energy as that obtained from the MC simulation. The temperatures clearly vary non-monotonically with bias, and may be quite different for the HH1 and LH1 subbands. The hole temperatures are generally well above the lattice temperature, which is related to the fact that the bias in this structure has to be rather large.

The actual hole distributions in the HH1 and LH1 subbands are shown in Figs. 3(a) and 3(b) for two different values of bias, one below and the other above the alignment

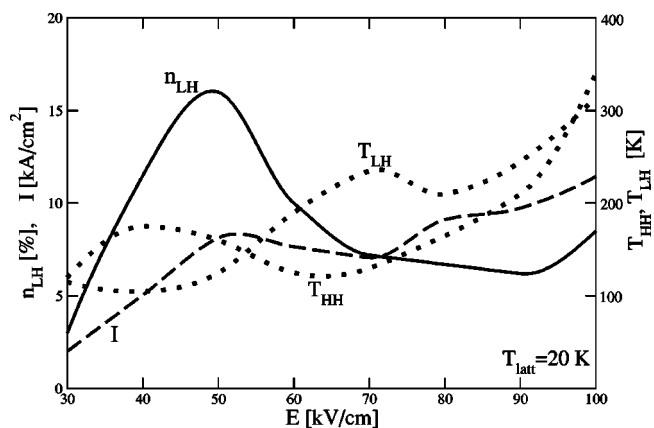


FIG. 2. The LH1 subband population (solid), the current density (dashed), and the effective temperatures of the HH1 and LH1 subbands (dotted lines), vs electric field in the  $p$ -Si/SiGe cascade shown in Fig. 1, calculated using the MC method. The lattice temperature  $T_{\text{latt}}$  is 20 K, and the sheet hole density  $5 \times 10^{11} \text{ cm}^{-2}$  per period.

bias. Also shown are the FD distributions calculated for the subband effective temperatures shown in Fig. 2. The actual distributions clearly differ in shape from the FD form. A common feature is that the HH1 distribution has an overshoot around  $\mathbf{k}_{\parallel}=0$  and then falls off rather steeply, but a number of hot holes still remain. In contrast, the LH1 subband distribution appears broadened when compared to the FD distribution for this subband. Both effects may be attributed to the state mixing properties of hole quantized states. At  $\mathbf{k}_{\parallel}=0$  the HH1 subband is purely hh-like in character, while the lh and so admixtures increase with increasing  $\mathbf{k}_{\parallel}$ . Similarly, the LH1 subband is lh-like in character (with some content of so) at  $\mathbf{k}_{\parallel}=0$ , while the hh admixture increases for  $\mathbf{k}_{\parallel}$  away from this point. The confined state wave function decays in the Si barriers, but the decay is slower for the lh than the hh component. This is because the hh effective mass in the perpendicular direction is somewhat larger than the lh mass (though not very much in Si-abundant SiGe), and the hh band discontinuity is larger, since the SiGe well material has compressive strain, while the Si barriers have tensile strain. Therefore, the HH1 state is best confined in the well near  $\mathbf{k}_{\parallel}=0$ , and the LH1 state confinement increases away from  $\mathbf{k}_{\parallel}=0$ . Consequently, with the smallest overlap with states from the adjacent periods, the retention time of HH1 states near  $\mathbf{k}_{\parallel}=0$  is largest, hence their abundance in the distribution function. The opposite argument applies for the LH1 distribution. It is interesting to note a similar observation regarding hole tunneling from the (heavy-hole) ground state of GaAs/AlGaAs based quantum wells: it occurs mostly via the light-hole component of the wave function.<sup>51</sup> If hole-hole scattering was included in the calculation, one would expect the distribution profiles to become more FD-like, because this scattering tends to drive the distribution towards its equilibrium form<sup>52</sup> (with a temperature unrelated to the lattice temperature, however). An increased interwell total scattering rate would then also lead to increased current density, and would therefore heat the hole distributions further above the values predicted here.

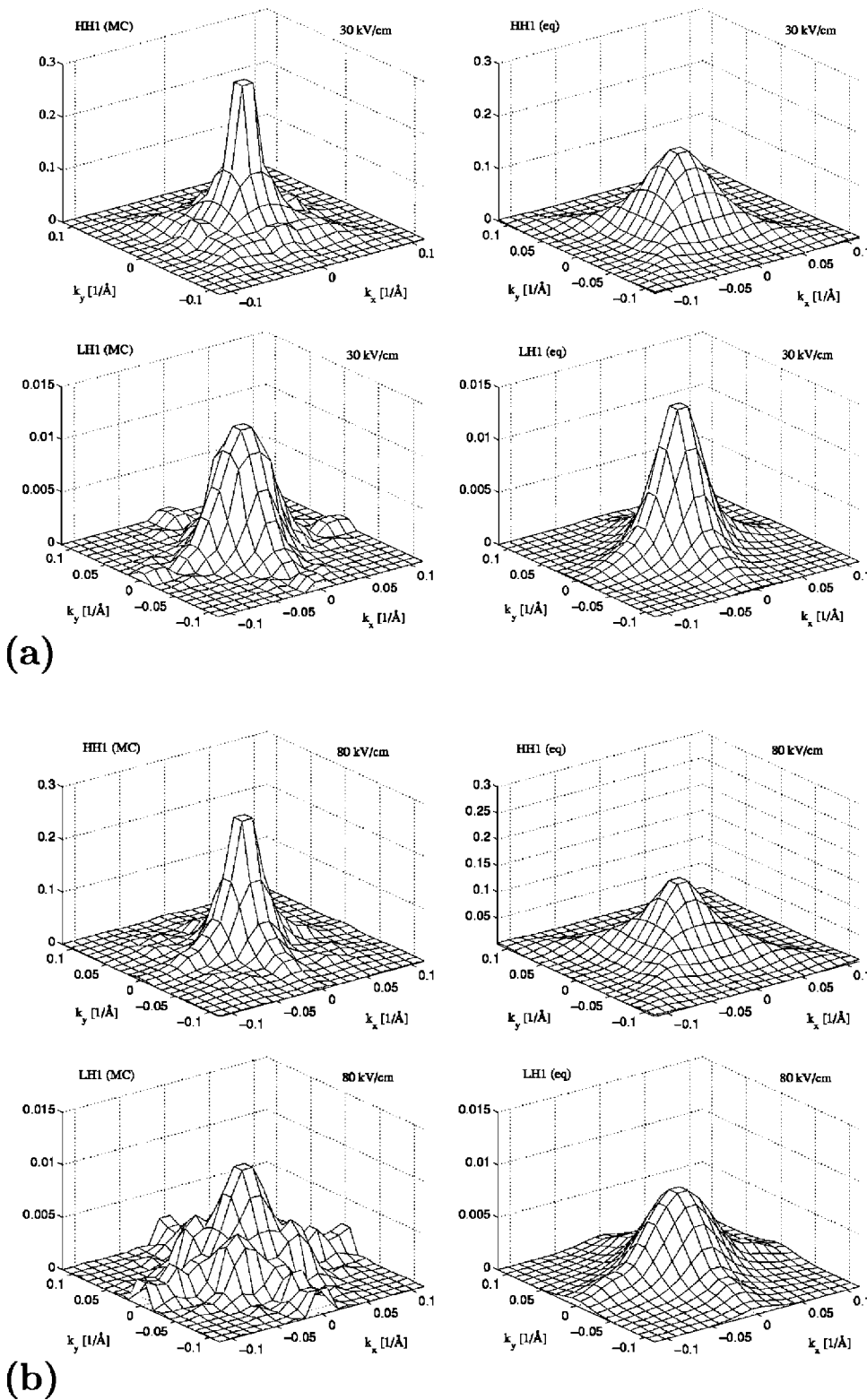


FIG. 3. The MC generated (label MC) steady-state hole distributions (on the left) for the HH1 and LHI subbands in the *p*-Si/SiGe cascade shown in Fig. 1, with (a) 30 kV/cm, and (b) 80 kV/cm bias. The lattice temperature  $T_{latt}$  is 77 K. The quasi-equilibrium FD distributions (label eq) corresponding to the carrier temperatures shown in Fig. 2 are given on the right for comparison.

An alternative type of *p*-Si/SiGe cascade structure was considered, which was designed to have an inverted-mass (or negative-mass) feature. This appears when two subbands happen to be almost degenerate for some  $k_{||}$  (usually at  $k_{||} = 0$ ), giving rise to a strong interaction which “repels” the bands in energy space, such that the lower of the two bends downwards in energy as  $k_{||}$  increases, creating the inverted

mass feature. Once the two states are sufficiently apart, their interaction weakens and both acquire the normal, positive-mass dispersion. For this mechanism to be possible, one of the states should be hh and the other lh in character, e.g., LHI and HH2. The net effect is a subband with an energy minimum at some finite  $k_{||}$ , Fig. 4. This type of structure has been proposed as a possible intersubband laser, based on a

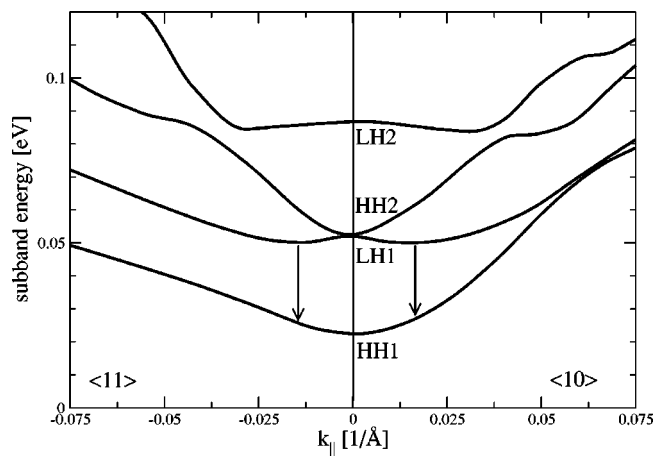


FIG. 4. The hole subbands' dispersion along the  $\langle 10 \rangle$  and  $\langle 11 \rangle$  in-plane directions in a 38 monolayer (10.47 nm)  $\text{Ge}_{0.3}\text{Si}_{0.7}$ /19 monolayer (5.13 nm) Si cascade on  $\text{Ge}_{0.2}\text{Si}_{0.8}$  virtual substrate, with the inverted-mass feature in the second subband. The arrows denote optical transitions where a local population inversion is expected.

local-in- $\mathbf{k}$ -space, rather than a global, population inversion,<sup>53,54</sup> and has also been discussed specifically for the  $p$ -Si/SiGe system.<sup>55,56</sup> The rationale was that holes in the upper laser state, which is the subband with the negative mass feature, should accumulate around the minimum at  $\mathbf{k}_{\parallel 0}$ , while those in the lower laser state, which is a lower subband with normal dispersion (HH1), accumulate around the band minimum at  $\mathbf{k}_{\parallel} = 0$ . At the same time the HH1 states around  $\mathbf{k}_{\parallel 0}$  should be almost empty, creating a local population inversion around  $\mathbf{k}_{\parallel 0}$  (this is a ring in the the 2D  $\mathbf{k}_{\parallel}$  plane, although not exactly circular because of anisotropy). Gain might thus appear for photon energies around  $E_{LH1}(\mathbf{k}_{\parallel 0}) - E_{HH1}(\mathbf{k}_{\parallel 0})$  (indicated by arrows in Fig. 4), even though there may be no global population inversion between the LH1 and HH1 subbands.

An inverted-mass feature can be engineered in a strain-balanced cascade comprising 38 monolayer (10.47 nm)  $\text{Ge}_{0.3}\text{Si}_{0.7}$  wells and 19 monolayer (5.13 nm) Si barriers, grown on a  $\text{Ge}_{0.2}\text{Si}_{0.8}$  virtual substrate. The local minimum of the upper subband occurs at  $\mathbf{k}_{\parallel 0} = 0.015 \text{ \AA}^{-1}$ , and is about 3 meV below the energy at  $\mathbf{k}_{\parallel} = 0$ . Although the above description suggests that it suffices to consider just the two working subbands per period of the cascade—HH1 and LH1 in this instance—it is strictly necessary to include HH2 and LH2 as well. HH2 should be included because it is almost degenerate with LH1 at  $\mathbf{k}_{\parallel} = 0$ , and there may be non-negligible scattering to/from it. The LH2 subband should be included since one peculiarity of the Si/SiGe system is that the LH2-LH1 spacing is similar to the HH2-HH1 spacing, due to the effective masses and band offsets mentioned above. Therefore, just as the HH1 subband of the preceding period injects holes into the LH1 and HH2 subbands of the next period, so do these two subbands inject carriers into the LH2 subband of the subsequent period.

The results of MC simulations performed for this structure are given in Fig. 5. The alignment of the HH1 subband from the preceding period with the LH1 subband of the next occurs at a bias of 19 kV/cm. The population of the LH1

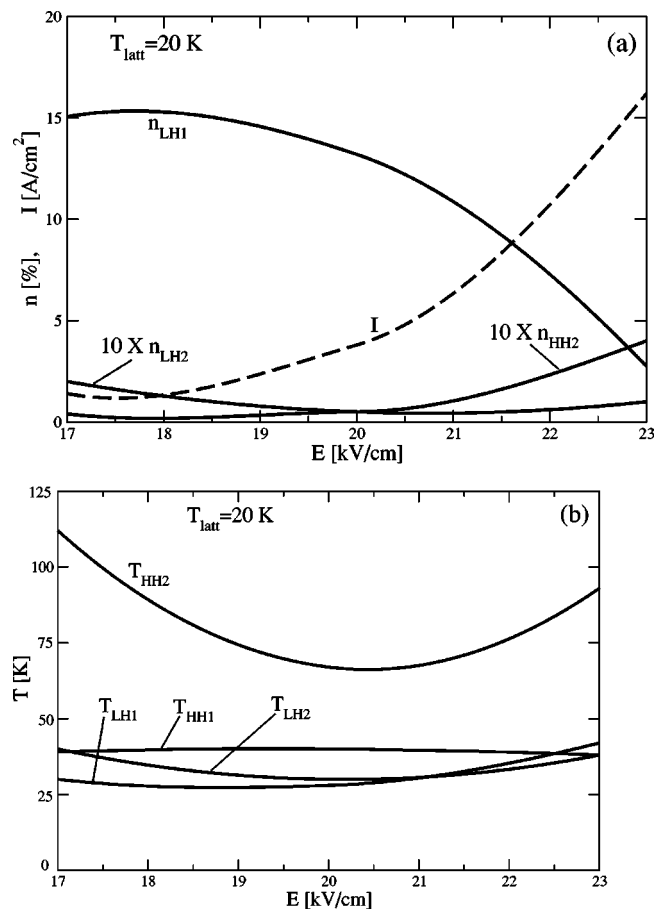


FIG. 5. (a) The subband populations (solid) and current density (dashed) and (b) the effective temperatures, vs electric field in the quantum cascade structure described in Fig. 4. The lattice temperature  $T_{\text{latt}}$  is 20 K, and the sheet hole density  $1 \times 10^{11} \text{ cm}^{-2}$  per period.

subband has a very broad peak in this range, never exceeding that of the HH1 subband, but this is not required for this system. The population of the upper two subbands (HH2 and LH2) is found to be very small after all, because of their larger energies (hence the optical phonon scattering becomes fast). The hole temperatures are considerably lower than for the interwell cascade described previously. This is due to a lower bias, and a much lower current (the barriers are much thicker than in the previous example, which makes interwell scattering slow), so holes do not have to be heated much above the lattice temperature in order to dissipate the input power. These are generally favorable conditions for carrier thermalization, i.e., settling around the local minima in both the upper and lower laser states. Another beneficial feature is the absence of NDR in the range of biases of interest; i.e., no domain formation is to be expected in this structure. Figure 6 shows the calculated hole distributions in the two lowest subbands for 20 kV/cm and 23 kV/cm bias. These show that there is a small local population inversion around a few “islands” in the  $\mathbf{k}_{\parallel}$  plane at 20 kV/cm [and generally around the HH1(L)-LH1 alignment bias], but the inversion disappears further away from the alignment bias, e.g., for a field of 23 kV/cm. However, if the subband populations and hole

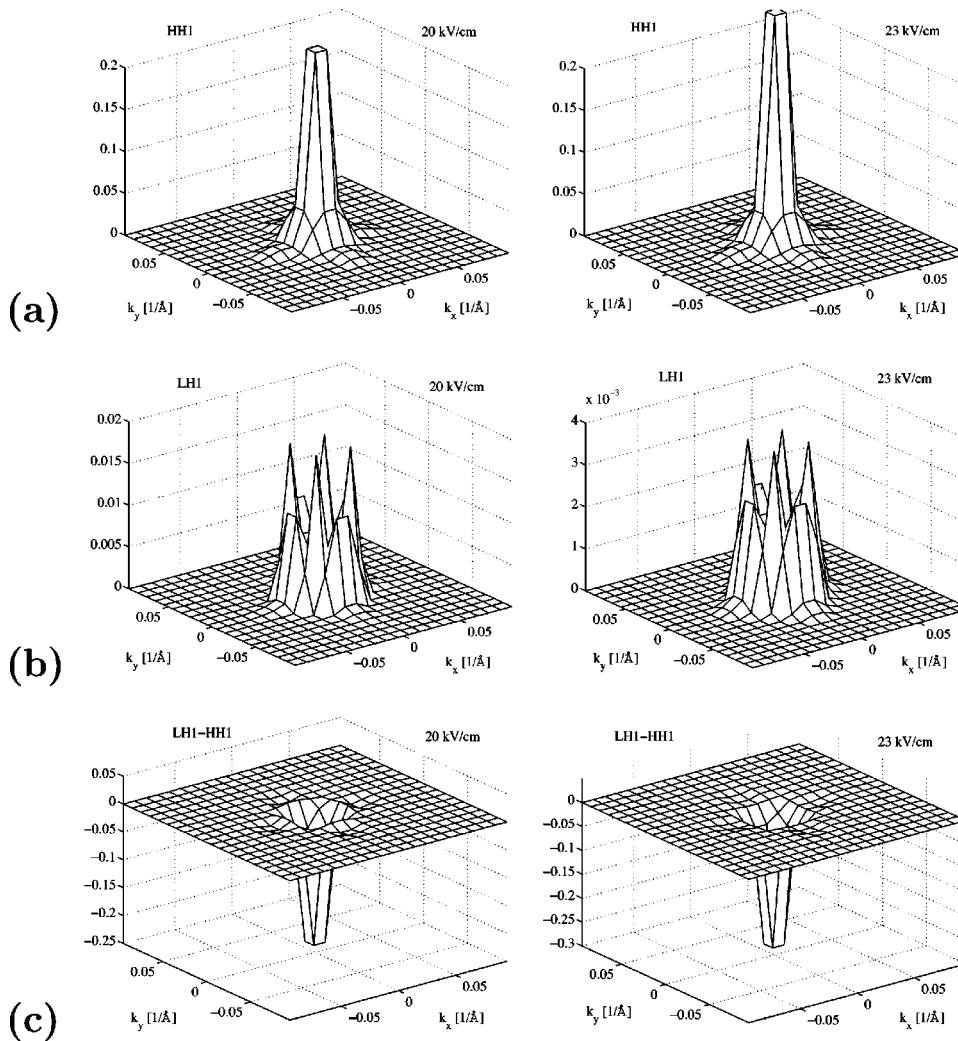


FIG. 6. The MC generated hole distributions for the (a) HH1 and (b) LH1 subband, and (c) the population inversion in the inverted-mass *p*-SiGe cascade described in Fig. 5 at 20 and 23 kV/cm bias.

temperatures found in the MC simulation are used in FD distributions, there would be no inversion at all. Therefore, the inversion is largely due to the “condensation” of holes around  $\mathbf{k}_{\parallel}=0$  in the HH1 subband (the effect described in the previous example), because the effective hole temperature in the LH1 subband is still too high, and the local minimum of the LH1 subband is too shallow for any significant carrier accumulation to occur in this region due to temperature alone. In view of the fact that hole-hole scattering, if included, would drive the distributions towards their equilibriumlike forms, and would make the carrier temperatures both higher and closer to each other,<sup>57</sup> one may infer that it would probably further diminish, if not completely destroy, the fragile inversion found in the present simulation.

Another set of calculations was performed for an inverted-mass cascade comprising 34 monolayer  $\text{Ge}_{0.43}\text{Si}_{0.57}$  wells and 12 monolayer Si barriers, grown on a  $\text{Ge}_{0.3}\text{Si}_{0.7}$  virtual substrate. The barriers in this design are considerably thinner and, despite the deeper wells, this results in a larger current and larger carrier temperatures, so the structure was found to be very remote from achieving a local population inversion, as might have been expected.

The main obstacle for larger inversion in inverted-mass structures is the shallowness of the energy minimum in the

upper subband ( $\leq 3$  meV for the LH1/HH2 degenerate set). The HH-LH subband coupling is determined by the  $\gamma_3$  Luttinger parameter, which is relatively small in the Si-abundant SiGe. Using pure Ge wells (or GaAs/AlGaAs heterostructures) would improve the situation in this respect. An alternative approach could involve using higher subbands, because this produces deeper inverted-mass minima. However, with a larger range of energies involved, the holes would encounter more complex and much faster intersubband dynamics, due to optical phonon scattering, which would reduce the lifetime of states in the local minimum, and hence mitigate against population inversion.

#### IV. CONCLUSION

Hole transport in *p*-Si/SiGe quantum-cascade structures was studied using ensemble Monte Carlo simulation that includes the alloy disorder, acoustic and optical phonon scattering, accounting for the anisotropy of the subband structure and the scattering rates. It does not assume any functional form for the carrier distribution, but instead derives the distributions directly from an ensemble average of the states of the simulated devices. This is an advantage of the MC approach over rate-equation models, particularly valuable for

$p$ -type structures because their electronic and optical properties are more sensitive to the carrier distribution than is the case in  $n$ -type cascades.

Simulations have been carried out for two types of prototype THz Si/SiGe strain-balanced quantum cascade structures. In structures designed to achieve local population inversion around an inverted mass feature in the LH1 subband, only marginal inversion was found, which is likely to be destroyed in the presence of hole-hole scattering. The main reason for the poor inversion is the shallowness of the energy minimum in the LH1 dispersion. However, substantial population inversion was predicted in  $p$ -Si/SiGe cascades designed to operate via interwell (diagonal) radiative transitions between the ground (HH1) subband of one well and the upper (LH1) subband of the next well. Despite the high car-

rier temperatures, the population inversion exists across a wide range of applied biases, with over 90% of carriers in the upper laser subband at the desired operating point. These results imply that such heterostructures have strong potential for Si/SiGe quantum cascade laser action, although it should be noted that the calculations presented here do not account for any domain formation which may occur in many-period heterostructures.

#### ACKNOWLEDGMENTS

This work was supported by DARPA/ USAF Contract No. F19628-99-C-0074. The authors thank R. A. Soref (Hanscom AFB) for useful discussions.

\*Email address: eenzi@leeds.ac.uk

- <sup>1</sup>R. A. Soref, L. Friedman, and G. Sun, *Superlattices Microstruct.* **23**, 427 (1998).
- <sup>2</sup>L. Friedman, R. A. Soref, G. Sun, and Y. Lu, *IEEE J. Sel. Top. Quantum Electron.* **4**, 1029 (1998).
- <sup>3</sup>G. Dehlinger, L. Diehl, U. Gennser, H. Sigg, J. Faist, K. Ensslin, D. Grützmacher, and E. Müller, *Science* **290**, 2277 (2000).
- <sup>4</sup>L. Diehl, S. Mentese, E. Müller, D. Grützmacher, H. Sigg, U. Gennser, I. Sagnes, Y. Campidelli, O. Kermarrec, D. Bensahel, and J. Faist, *Appl. Phys. Lett.* **81**, 4700 (2002).
- <sup>5</sup>S. A. Lynch, R. Bates, D. J. Paul, D. J. Norris, A. G. Cullis, Z. Ikonić, R. W. Kelsall, P. Harrison, D. D. Arnone, and C. R. Pidgeon, *Appl. Phys. Lett.* **81**, 1543 (2002).
- <sup>6</sup>D. J. Paul, S. A. Lynch, R. Bates, Z. Ikonić, R. W. Kelsall, P. Harrison, D. J. Norris, S. L. Liew, A. G. Cullis, D. D. Arnone, C. R. Pidgeon, P. Murzyn, J. P. R. Wells, and I. V. Bradley, *Physica E (Amsterdam)* **16**, 147 (2003).
- <sup>7</sup>R. Bates, S. A. Lynch, D. J. Paul, Z. Ikonić, R. W. Kelsall, P. Harrison, S. L. Liew, D. J. Norris, A. G. Cullis, W. R. Tribe, and D. D. Arnone, *Appl. Phys. Lett.* **83**, 4092 (2003).
- <sup>8</sup>P. Rauter, T. Fromherz, G. Bauer, L. Diehl, G. Dehlinger, H. Sigg, D. Grützmacher, and H. Schneider, *Appl. Phys. Lett.* **83**, 3879 (2003).
- <sup>9</sup>K. Donovan, P. Harrison, and R. W. Kelsall, *J. Appl. Phys.* **89**, 3084 (2001).
- <sup>10</sup>K. Kalna, C. Y. L. Cheung, and K. A. Shore, *J. Appl. Phys.* **89**, 2001 (2001).
- <sup>11</sup>D. Indjin, P. Harrison, R. W. Kelsall, and Z. Ikonić, *J. Appl. Phys.* **91**, 9019 (2002).
- <sup>12</sup>D. Indjin, P. Harrison, R. W. Kelsall, and Z. Ikonić, *Appl. Phys. Lett.* **81**, 400 (2002).
- <sup>13</sup>D. Indjin, P. Harrison, R. W. Kelsall, and Z. Ikonić, *IEEE Photonics Technol. Lett.* **15**, 15 (2003).
- <sup>14</sup>S. Barbieri, F. Beltram, and F. Rossi, *Phys. Rev. B* **60**, 1953 (1999).
- <sup>15</sup>R. C. Iotti and F. Rossi, *Appl. Phys. Lett.* **78**, 2902 (2001).
- <sup>16</sup>R. C. Iotti and F. Rossi, *Phys. Rev. Lett.* **87**, 146603 (2001).
- <sup>17</sup>R. Köhler, R. C. Iotti, A. Tredicucci, and F. Rossi, *Appl. Phys. Lett.* **79**, 3920 (2001).
- <sup>18</sup>R. C. Iotti and F. Rossi, *Phys. Status Solidi B* **238**, 462 (2003).
- <sup>19</sup>H. Callebaut, S. Kumar, B. S. Williams, Q. Hu, and J. L. Reno, *Appl. Phys. Lett.* **83**, 207 (2003).
- <sup>20</sup>R. W. Kelsall, P. Kinsler, and P. Harrison, *Physica E (Amsterdam)* **7**, 48 (2000).
- <sup>21</sup>R. Oberhuber, G. Zandler, and P. Vogl, *Phys. Rev. B* **58**, 9941 (1998).
- <sup>22</sup>M. V. Fischetti, Z. Ren, P. M. Solomon, M. Yang, and K. Rim, *J. Appl. Phys.* **94**, 1079 (2003).
- <sup>23</sup>Z. Ikonić, P. Harrison, and R. W. Kelsall, *Phys. Rev. B* **64**, 245311 (2001).
- <sup>24</sup>B. A. Foreman, *Phys. Rev. B* **48**, 4964 (1993).
- <sup>25</sup>Z. Ikonić, P. Harrison, and R. W. Kelsall, *Phys. Rev. B* **64**, 125308 (2001).
- <sup>26</sup>M. El kurdi, G. Fishman, S. Sauvage, and P. Boucaud, *Phys. Rev. B* **68**, 165333 (2003).
- <sup>27</sup>K. Bhaumik, B. K. Ridley, and Y. Shacham-Diamand, *J. Appl. Phys.* **74**, 5546 (1993).
- <sup>28</sup>F. L. Madarasz and F. Szmulowicz, *Phys. Rev. B* **24**, 4611 (1981).
- <sup>29</sup>F. Szmulowicz, *Phys. Rev. B* **28**, 5943 (1983).
- <sup>30</sup>J. M. Hinckley and J. Singh, *J. Appl. Phys.* **76**, 4192 (1994).
- <sup>31</sup>K. Reimann, R. A. Kaindl, and M. Woerner, *Phys. Rev. B* **65**, 045302 (2001).
- <sup>32</sup>K. Greipel and U. Rössler, *Semicond. Sci. Technol.* **7**, 487 (1992).
- <sup>33</sup>D. C. Look, D. K. Lorance, J. R. Sizelove, C. E. Stutz, K. R. Evans, and D. W. Whitson, *J. Appl. Phys.* **71**, 260 (1992).
- <sup>34</sup>K. Yeom, J. M. Hinckley, and J. Singh, *J. Appl. Phys.* **80**, 6773 (1996).
- <sup>35</sup>M. J. Kearney and A. I. Horrell, *Semicond. Sci. Technol.* **13**, 174 (1998).
- <sup>36</sup>G. Gilat and N. R. Bharatiya, *Phys. Rev. B* **12**, 3479 (1975).
- <sup>37</sup>S.-Y. Ren and W. A. Harrison, *Phys. Rev. B* **23**, 762 (1981).
- <sup>38</sup>S. I. Kurganskii, O. I. Dubrovskii, and E. P. Domashevskaya, *Phys. Status Solidi B* **129**, 293 (1985).
- <sup>39</sup>H. Eschrig, *Optimized LCAO-Method* (Springer-Verlag, Berlin, 1989), Chap. 6, pp. 113–219.
- <sup>40</sup>K. Kometer, G. Zandler, and P. Vogl, *Phys. Rev. B* **46**, 1382 (1992).
- <sup>41</sup>M. A. Alam and M. S. Lundstrom, *Appl. Phys. Lett.* **67**, 512

- (1995).
- <sup>42</sup>M. Saraniti and S. M. Goodnick, *IEEE Trans. Electron Devices* **47**, 1909 (2000).
- <sup>43</sup>S. M. Goodnick and P. Lugli, *Phys. Rev. B* **37**, 2578 (1988).
- <sup>44</sup>M. V. Fischetti and S. E. Laux, *Phys. Rev. B* **38**, 9721 (1988).
- <sup>45</sup>R. Rovatti, M. Borgatti, and R. Guerrieri, *IEEE Trans. Comput.* **47**, 894 (1998).
- <sup>46</sup>P. Lugli and D. K. Ferry, *IEEE Trans. Electron Devices* **ED-32**, 2431 (1985).
- <sup>47</sup>S. C. Lee and I. Galbraith, *Phys. Rev. B* **75**, 16025 (1997).
- <sup>48</sup>A. Kahan, M. Chi, and L. Friedman, *J. Appl. Phys.* **75**, 8012 (1994).
- <sup>49</sup>C. G. Van de Walle and R. M. Martin, *Phys. Rev. B* **34**, 5621 (1986).
- <sup>50</sup>P. Murzyn, C. R. Pidgeon, J.-P. R. Wells, I. V. Bradley, Z. Ikonić, R. W. Kelsall, P. Harrison, S. A. Lynch, D. J. Paul, D. D. Arnone, D. J. Robbins, D. J. Norris, and A. G. Cullis, *Appl. Phys. Lett.* **80**, 1456 (2002).
- <sup>51</sup>A. G. Petrov and A. Shik, *J. Appl. Phys.* **83**, 3203 (1998).
- <sup>52</sup>D. K. Ferry, S. M. Goodnick, and K. Hess, *Physica B* **272**, 538 (1999).
- <sup>53</sup>G. Sun, Y. Lu, and J. B. Khurgin, *Appl. Phys. Lett.* **72**, 1481 (1998).
- <sup>54</sup>G. Sun and Y. Lu, *Opt. Express* **2**, 143 (1998).
- <sup>55</sup>L. Friedman, G. Sun, and R. A. Soref, *Appl. Phys. Lett.* **78**, 401 (2001).
- <sup>56</sup>R. A. Soref and G. Sun, *Appl. Phys. Lett.* **79**, 3639 (2001).
- <sup>57</sup>P. Harrison, *Appl. Phys. Lett.* **75**, 2800 (1999).